

Scattering matrix elements of fractal-like soot agglomerates

S. Manickavasagam and M. P. Mengüç

The possibility of measuring scattering-matrix (Mueller matrix) elements of soot agglomerates with laser diagnostic techniques is explored. To show this, we calculated the scattering-matrix elements of arbitrary-shaped soot agglomerates. The sensitivity of scattering-matrix elements to optical and morphological characteristics of fractal-like soot agglomerates is discussed. Finally, possible measurement techniques are suggested to identify soot structures from scattering-matrix elements. © 1997 Optical Society of America

Key words: Scattering, matrix, soot, fractal-like, agglomerates.

1. Introduction

Soot is one of the most important contributors to radiative transfer and is formed during the combustion of almost all hydrocarbons. Unlike combustion gases such as H_2O or CO_2 , which absorb and emit only at certain wavelengths, soot participates in radiative transfer at all wavelengths. A sooty flame emits significantly more radiant energy than does a clean-burning natural-gas flame. Although this can be considered as an advantage, unburned carbon particles emitted at the exhaust of combustion chambers is a major drawback. To predict the contribution of soot to overall radiative transfer phenomena and to find ways to eliminate unburned carbon, one must know the details of soot formation, coagulation, and oxidation. These phenomena can be understood best using nonintrusive laser diagnostic techniques. The experimental data need to be reduced to obtain the information about the soot volume fraction distribution, which is possible only if an accurate accounting is made of the details of soot-particle and soot-agglomerate shape, structure, size, size distribution, and optical properties.

It is well known that individual soot particles formed in laboratory-scale flames are small compared with the wavelength of visible light and are spherical in shape.¹⁻³ It is generally accepted that the pri-

mary soot particles are spherical in shape and ~ 10 – 100 nm in diameter.⁴ As the formation of soot progresses, the primary soot particles agglomerate to become random clusters that may have a fractal-like or chainlike morphology owing to electrical charging and random collision.^{2,5} Coagulation among these agglomerates leads to more complex morphology that can have radiative properties significantly different from spheres. These changes in particle morphology have been observed using intrusive techniques in which the particles are sampled and then investigated under electron microscopes.⁵⁻⁷ To obtain accurate and detailed information about soot agglomeration and volume fraction under different combustion conditions, nonintrusive techniques such as laser diagnostics are essential in addition to intrusive measurements. Nonintrusive techniques require measuring relevant characteristics of the system and interpreting the data with available theoretical models such as inverse analyses.

Sorensen *et al.*⁸ have presented a technique to measure the soot-agglomerate characteristic nonintrusively with laser diagnostic techniques. They could not, however, accurately obtain the number of primary spheres and the size of the primary sphere in an agglomerate. Köylü and Faeth⁹ have extended this approach and evaluated various approximate models for the radiative properties of soot agglomerates. Their results indicate that the uncertainties in determining the characteristics of soot agglomerates still remain. It is worth noting that the sizes of soot agglomerates vary, and for a polydispersed system of agglomerates determination of the size and number of primary spheres is more difficult than determination for a monodispersed cloud.

The authors are with the Department of Mechanical Engineering, University of Kentucky, Lexington, Kentucky 40506.

Received 24 August 1995; revised manuscript received 8 August 1996.

0003-6935/97/061337-15\$10.00/0

© 1997 Optical Society of America

In this paper we explore the possibility of eliminating these uncertainties by measuring scattering-matrix (Mueller matrix) elements of soot agglomerates. Mueller matrix elements provide all the information about the scattering characteristics of a soot particle or a soot agglomerate.¹⁰ If we measure these matrix elements, it is possible to identify soot-agglomerate characteristics *in situ* because, as is shown below, these elements are sensitive to the variations in morphology and refractive index of the scatterer.

A recently developed computer program, AGGLOME, was used to calculate the scattering-matrix elements of arbitrary-shaped soot agglomerates. First, the electromagnetic wave propagation inside a soot agglomerate is modeled with the principles of the volume-integral equation formulation and the method of moments (Iskander *et al.*¹¹). Then we performed orientational averaging and obtained scattering-matrix elements using a similar procedure.¹²

First we outline the theoretical model employed and present the scattering-matrix elements obtained. The model is evaluated against spherical-particle results obtained from Lorenz-Mie theory. We also discuss the sensitivity of these elements to optical and morphological characteristics of fractal-like soot agglomerates. Finally, we comment on the possible measurement techniques that one can use to identify soot structures using scattering-matrix elements. To our knowledge, there is no other study in the literature that discusses the possible use of these elements for soot diagnostics. Only the study of Singham and Salzman¹² presented a set of similar results for spherical and irregular-shaped particles (but not agglomerates).

2. Review of Agglomerate Models

If soot particles in hydrocarbon flames are not agglomerated, estimation of soot-volume fraction is straightforward. Because the size of an individual soot sphere is usually much smaller than the wavelength of incident radiation used for laser diagnostics, the Rayleigh limit to Lorenz-Mie theory can be used (for small $x = \pi D/\lambda$). On the other hand the scattering characteristics of soot agglomerates are quite different from those of Rayleigh spheres because of their large size and irregular shape. We present a brief overview of studies that have appeared in the literature for modeling the scattering of light by irregular particles and agglomerates.

Determining the scattering characteristics of an agglomerate is more complicated than determining scattering characteristics for a homogeneous but irregular-shaped particle. For the latter one can obtain a solution by matching the amplitude and phase of the electromagnetic waves inside and outside the particle, which is mathematically difficult but straightforward. For agglomerates, however, the interaction between individual spheres should be accounted for by considering the superposition of elec-

tric field components of scattered electromagnetic waves from each individual sphere.

Coherent scattering of radiation by soot agglomerates has been studied by various researchers. The first model developed to examine irregular-shaped particles and agglomerates in a comprehensive way, including the retardation effects, was the discrete-dipole approximation (DDA) of Purcell and Pennypacker,¹³ who used it to study interstellar dust. The DDA is a general and flexible method for computing the approximate extinction and scattering cross sections of particles of arbitrary shape. The particle is modeled by an array of N polarizable elements (called dipoles) in vacuum. The spacing between the dipoles is assumed to be small compared with the wavelength of incident radiation. Once the location of dipoles is determined, their interaction with the incident electromagnetic field as well as with electromagnetic fields scattered by the neighboring dipoles can be formulated. This yields a set of linear algebraic equations that can be solved using standard procedures in the literature. The resultant field at each dipole is determined from the solution of these equations. The scattering, absorption, and extinction efficiencies are then calculated.

In their original study, Purcell and Pennypacker presented solutions for particles with $N < 256$. However, they encountered difficulties with convergence of the iterative scheme they employed to solve the governing equations. Shapiro¹⁴ used the DDA to calculate the optical properties of brick-shaped magnetite grains (with $N = 128$) and employed a matrix inversion scheme for the solution of the set of linear equations, which was suitable only for small values of N . The DDA was subsequently applied to inhomogeneous spheroids (with $N = 389$) by Druger *et al.*¹⁵ and was used by Kattawar and Humphreys¹⁶ to compute scattering from two neighboring spheres (with $N = 64$). Yung,¹⁷ using a new iterative method to solve the linear equations, calculated cross sections for spheres with N as large as 15,600. This algorithm, however, failed to converge for strongly absorbing particles.

The DDA was also applied to inhomogeneous particles, as well as chiral particles such as a simple helix, a helical ribbon, and a twisted ladder.¹⁸⁻²⁰ Varadan *et al.*²¹ extended the DDA to compute the scattering characteristics of anisotropic objects by considering a uniaxial sphere made of titanium dioxide. Nonspherical subunits were considered by Singham and Salzman¹² and by Varadan *et al.*²¹ Agglomerates of distinct particles were modeled and the feasibility of recovering the fractal dimension of self-similar agglomerates from backscattered measurements has been demonstrated.²² A different version of this approach was investigated by Singham and Bohren²³ and Dungey and Bohren.²⁴ Draine²⁵ presented a comprehensive treatment of the problem and discussed the validity of various approximations. A compilation of the papers on the fundamentals and applications of the DDA was given by Lakhtakia.²⁶ Later extensions of this approach

were discussed by Hage and Greenberg²⁷ and Flatau *et al.*²⁸ Mengüç *et al.*²⁹ modeled radiative properties of soot agglomerates using the discrete-dipole method of Draine and observed gradual variation in the agglomerate shape along the axis of a diffusion flame. A detailed review of DDA for scattering calculations and its relation to the other methods was presented by Draine *et al.*³⁰

Recently a new approach to predict scattering and absorption coefficients of multiple-sphere clusters was presented by Mackowski³¹ and Fuller³² who considered the superposition of radiative interactions among spheres. Analytical expressions were derived for orientation-averaged scattering and absorption coefficients. These expressions would serve as valuable tools for laser diagnostic techniques such as transmission tomography. However, they are not readily usable in inverse analysis of experimentally measured total-scattered intensities or other quantities such as Mueller matrix elements. It was reported by Mackowski³¹ that the derivation of analytical expressions for orientationally averaged differential-scattering cross sections was difficult and, even if possible, the algorithm might be computationally time-consuming. Fuller³² employed his algorithm to evaluate the absorption and scattering coefficients for various two-sphere cases and for multisphere clusters; the computational time requirements were not reported.

The solution of governing equations of a DDA requires the inversion of a matrix of considerably large dimensions. To ease this problem, Draine²⁵ used a conjugate gradient method to minimize the errors introduced by the matrix-inversion algorithms. Flatau *et al.*²⁸ exploited the geometric symmetries of particles and the incident field in order to reduce the storage requirements necessary for solving the system of equations. However, with the availability of high-speed computers, these problems will likely be avoided. Given its flexibility, the discrete-dipole approximation can be used effectively to investigate different types of soot agglomerates and the changes in their structures as a function of flame conditions.

For agglomerates of small spheres, a solution technique developed by Jones^{33,34} received considerable attention in the past (Felske *et al.*,³⁵ Drolen and Tien,³⁶ Kumar,³⁷ Mackowski *et al.*,³⁸ Ku and Shim,^{39,40} and Charalampopoulos and Chang⁴¹). In this approach, the primary soot particles are assumed to be in the Rayleigh limit. The electric field within a particular primary soot particle is considered uniform and the field outside the particles is formulated with the integral formulation of the Maxwell equations. The accuracy of this model decreases significantly as the individual soot spheres become larger compared with the wavelength of radiation, that is, when they cannot be considered as Rayleigh spheres. Note that even for primary soot particles as small as 50 nm in diameter, the Rayleigh theory yields errors for the visible light, especially in the interpretation of the scattering of polarized light.

In another model proposed by Iskander *et al.*,¹¹ an

irregular-shaped particle was divided into a number of cubical cells and inside each cell the electromagnetic field was assumed to be uniform. Then a control volume approach was employed to reduce the governing equations to a set of linear algebraic equations. While deriving these equations, the interaction between various cubical cells was also considered. The governing equation obtained to determine the electric fields for the cubical cells is also valid for the spherical cells of the same volume.

Ku and Shim⁴⁰ used the formulations of Purcell and Pennypacker,¹³ Jones,^{33,34} and Iskander *et al.*¹¹ to model different-shaped soot agglomerates; and they compared the extinction coefficient, single-scattering albedo, and the phase function of agglomerates determined from these three approaches. They used the length of the cylinder to determine the overall size parameter and suggested its use for general models. However, the definition of the length scale for the overall size parameter does not seem to be solid and needs more research. They concluded that, among all the available techniques, the approach given by Iskander *et al.*¹¹ is the most versatile and reliable. Their results show that the scattering coefficient and the phase function of soot agglomerates are strongly dependent on the overall size parameter and the number of individual spheres that make the agglomerate.

Fractal representation of soot-agglomerate shapes has also been investigated to determine the corresponding radiative properties.^{41–45} From these studies, soot agglomerates were found to possess fractal-like structures that obey the relation

$$N = K_f \left(\frac{R_g}{2d_p} \right)^{D_f}, \quad (1)$$

where N is the number of primary spheres in the agglomerate, R_g is the radius of gyration of the agglomerate, d_p is the diameter of the primary sphere, K_f is the prefactor to be determined, and D_f is the fractal dimension of the agglomerate. Figure 1 shows different projections of two different fractal-like agglomerates, where N is either 25 or 125, and D_f is 1.7. The basic conclusion of these studies was that soot agglomerates have fractal dimensions of ~ 1.7 – 1.8 and a prefactor of 5.8. Recently Charalampopoulos⁴ presented a comprehensive review of the literature related to fractal representation of soot agglomerates. A consensus of all these studies is that the fractal geometry is better suited for the understanding of soot morphology and for the accurate interpretation of the data obtained from optical diagnostic techniques.

3. Theoretical Model

A. Formulation

In this section, we summarize the governing equations used to develop the computer program AGGLOME. Because this model is based on the volume-integral equation formulation and the method of moments

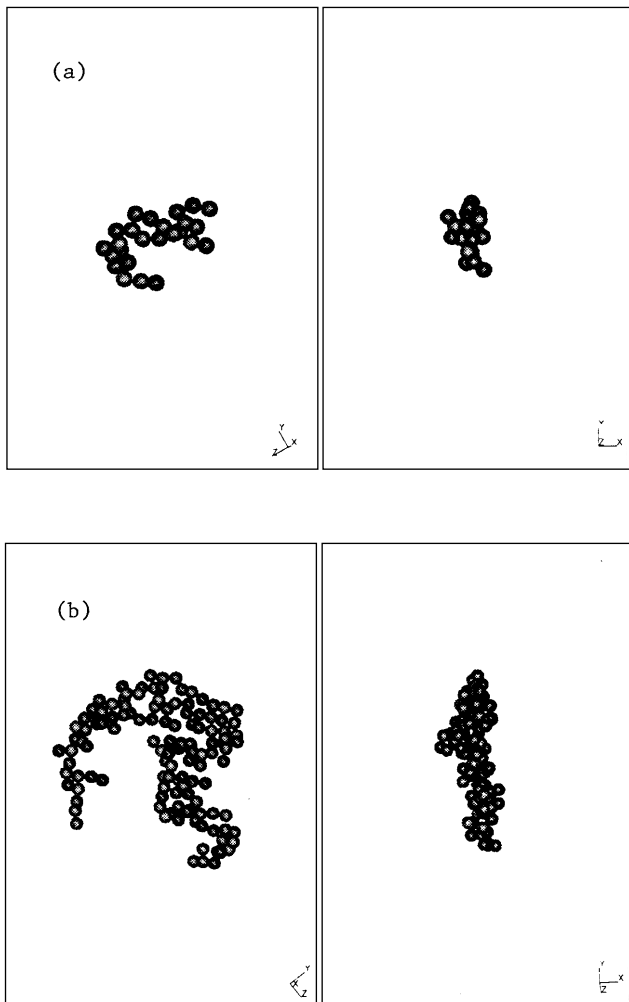


Fig. 1. Two soot-agglomerate models used, depicted at different orientations (fractal dimension of 1.7 with prefactor $k_f = 5.8$): (a) 25 spheres, (b) 125 spheres.

developed by Iskander *et al.*,¹¹ we do not discuss those details here.

We transformed the Maxwell equations for a lossy dielectric object into a system of linear algebraic equations by employing a control volume approach. If an electric field \mathbf{E}_{inc} that propagates along the z direction is incident on an arbitrary-shaped, fractal-like soot cluster, then the electric field in each primary cell (sphere) is expressed as

$$\mathbf{E}_i = \left(\frac{3}{\epsilon + 2} \right) \mathbf{E}_{\text{inc},i} + \frac{i}{3} \left(\frac{\epsilon - 1}{\epsilon + 2} \right) \sum_{j=1, j \neq i}^N x_j^3 \overleftrightarrow{T}_{ij} \mathbf{E}_j + s_i \mathbf{E}_i; \quad (2)$$

$$i = 1, 2, 3, \dots, N.$$

Here, k is the wave number ($k = 2\pi/\lambda$), R is the radius of the primary sphere, and $x_j = kR$ is the primary-sphere size parameter. The agglomerate is assumed to be formed of N primary spheres. For arbitrary-shaped particles, which are treated as com-

Table 1. Coefficients of Interaction Matrix

Coefficients	Expression
s_i	$2 \left(\frac{\epsilon - 1}{\epsilon + 2} \right) [\exp(ix_i)(1 - ix_i) - 1]$
a	$2h_0^{(1)}(\alpha) - h_2^{(1)}(\alpha)[P_2(\mu) - \frac{1}{2}\cos(2\psi)P_2^2(\mu)]$
a'	$2h_0^{(1)}(\alpha) - h_2^{(1)}(\alpha)[P_2(\mu) + \frac{1}{2}\cos(2\psi)P_2^2(\mu)]$
b	$\frac{1}{2}h_2^{(1)}(\alpha)\sin(2\psi)P_2^2(\mu)$
c	$-h_2^{(1)}(\alpha)\cos(\psi)P_2^1(\mu)$
d	$-h_2^{(1)}(\alpha)\sin(\psi)P_2^1(\mu)$
e	$2h_0^{(1)}(\alpha) + 2h_2^{(1)}(\alpha)P_2(\mu)$

posed of smaller cells of volume V_c , x_j is given as

$$x_j = k(3/4\pi)^{1/3}V_c^{1/3}. \quad (3)$$

The dielectric constant ϵ is given as $\epsilon = m^2$, m being the complex refractive index of the medium represented as $m = n + ik$, where $i = \sqrt{-1}$. Any variation in dielectric constant inside the agglomerate can be easily accounted for in the current formulation.

In Eq. (2), s_i is the coefficient for the self-interaction term, which needs careful consideration. The solution to the governing equation should satisfy the condition $C_e = C_a + C_{s,t}$, where C_e , C_a and $C_{s,t}$ are extinction, absorption, and total-scattering cross sections, respectively. For a single sphere and two-sphere cluster, this condition is satisfied only if the self-interaction term is included.^{40,46} The Jones formulation does not account for this term. Because the model formulated by Iskander *et al.*¹¹ satisfies this condition, it is more accurate than other available approaches, as observed by Ku and Shim.⁴⁰

If the incident field is given as

$$\mathbf{E}_{\text{inc},i} = E_0 \hat{e}_0 \exp(ikz_i), \quad (4)$$

we can normalize the irradiance of the incident field for the sake of simplicity:

$$I_0 = |E_0 \hat{e}_0|^2 = 1, \quad (5)$$

where \hat{e}_0 is the direction of the field vector. For linear polarization, \hat{e}_0 is a unit vector for either the x or y direction. The internal field vector \mathbf{E}_i is written as

$$\mathbf{E}_i = \begin{pmatrix} E_x \\ E_y \\ E_z \end{pmatrix}_i, \quad (6)$$

and the interaction matrix $\overleftrightarrow{T}_{ij}$ is defined as

$$\overleftrightarrow{T}_{ij} = \begin{pmatrix} a & b & c \\ b & a' & d \\ c & d & e \end{pmatrix}_{ij}. \quad (7)$$

The matrix elements a , b , c , d , e , and a' are identical to those given by Ku and Shim⁴⁰ and are outlined in Table 1.

The parameters required to evaluate these coeffi-

cients are

$$\begin{aligned}\alpha_{ij} &= kr_{ij} = (2\pi/\lambda)r_{ij}, \quad \mu_{ij} = (z_j - z_i)/r_{ij}, \\ \psi_{ij} &= \arctan[(y_j - y_i)/(x_j - x_i)], \\ h_0^{(1)}(\alpha) &= \frac{1}{\alpha} [\sin(\alpha) - i \cos(\alpha)], \\ t_1 &= \left(\frac{3}{\alpha^2} - 1\right) \sin(\alpha) - \frac{3}{\alpha} \cos(\alpha), \\ t_2 &= \left(1 - \frac{3}{\alpha^2}\right) \cos(\alpha) - \frac{3}{\alpha} \sin(\alpha), \\ h_2^{(1)}(\alpha) &= \frac{1}{\alpha} [(t_1) + i(t_2)], \quad P_2(\mu) = \frac{1}{2} (3\mu^2 - 1), \\ P_2^{-1}(\mu) &= -3\mu \sqrt{1 - \mu^2}, \quad P_2^2(\mu) = 3(1 - \mu^2).\end{aligned}$$

The governing equation, Eq. (2), is indeed a system of $3N \times 3N$ linear equations. It is expressed in scalar notation after replacement of the field vectors \mathbf{E}_i and $\mathbf{E}_{\text{inc},i}$ in terms of their components. After the tensor matrix \hat{T}_{ij} is expanded, Eq. (2) can be split into three different coupled linear systems of equations:

$$\begin{aligned}(1 - s_i)E_{x_i} - \frac{i}{3} \left(\frac{\epsilon - 1}{\epsilon + 2}\right) \sum_{\substack{j=1 \\ j \neq i}}^N x_j^3 (aE_{x_j} + bE_{y_j} + cE_{z_j}) \\ = \frac{3}{\epsilon + 2} E_{x_{\text{inc},i}} \quad i = 1, 2, 3, \dots, N.\end{aligned}\quad (8)$$

$$\begin{aligned}(1 - s_i)E_{y_i} - \frac{i}{3} \left(\frac{\epsilon - 1}{\epsilon + 2}\right) \sum_{\substack{j=1 \\ j \neq i}}^N x_j^3 (bE_{x_j} + a'E_{y_j} + dE_{z_j}) \\ = \frac{3}{\epsilon + 2} E_{y_{\text{inc},i}} \quad i = 1, 2, 3, \dots, N.\end{aligned}\quad (9)$$

$$\begin{aligned}(1 - s_i)E_{z_i} - \frac{i}{3} \left(\frac{\epsilon - 1}{\epsilon + 2}\right) \sum_{\substack{j=1 \\ j \neq i}}^N x_j^3 (cE_{x_j} + dE_{y_j} + eE_{z_j}) \\ = \frac{3}{\epsilon + 2} E_{z_{\text{inc},i}} \quad i = 1, 2, 3, \dots, N.\end{aligned}\quad (10)$$

We simplified these equations further by grouping like components together and modifying them into the following forms:

$$\begin{aligned}\sum_{\substack{j=1 \\ j \neq i}}^N \left[(1 - s_i)\delta - (1 - \delta) \frac{i}{3} \left(\frac{\epsilon - 1}{\epsilon + 2}\right) ax_j^3 \right] E_{x_j} \\ + \sum_{\substack{j=1 \\ j \neq i}}^N \left[-(1 - \delta) \frac{i}{3} \left(\frac{\epsilon - 1}{\epsilon + 2}\right) bx_j^3 \right] E_{y_j} \\ + \sum_{\substack{j=1 \\ j \neq i}}^N \left[-(1 - \delta) \frac{i}{3} \left(\frac{\epsilon - 1}{\epsilon + 2}\right) cx_j^3 \right] E_{z_j} \\ = \frac{3}{\epsilon + 2} E_{x_{\text{inc},i}} \quad i = 1, 2, 3, \dots, N,\end{aligned}\quad (11)$$

$$\begin{aligned}\sum_{\substack{j=1 \\ j \neq i}}^N \left[-(1 - \delta) \frac{i}{3} \left(\frac{\epsilon - 1}{\epsilon + 2}\right) bx_j^3 \right] E_{x_j} \\ + \sum_{\substack{j=1 \\ j \neq i}}^N \left[(1 - s_i)\delta - (1 - \delta) \frac{i}{3} \left(\frac{\epsilon - 1}{\epsilon + 2}\right) a'x_j^3 \right] E_{y_j} \\ + \sum_{\substack{j=1 \\ j \neq i}}^N \left[-(1 - \delta) \frac{i}{3} \left(\frac{\epsilon - 1}{\epsilon + 2}\right) dx_j^3 \right] E_{z_j} \\ = \frac{3}{\epsilon + 2} E_{y_{\text{inc},i}} \quad i = 1, 2, 3, \dots, N,\end{aligned}\quad (12)$$

$$\begin{aligned}\sum_{\substack{j=1 \\ j \neq i}}^N \left[-(1 - \delta) \frac{i}{3} \left(\frac{\epsilon - 1}{\epsilon + 2}\right) cx_j^3 \right] E_{x_j} \\ + \sum_{\substack{j=1 \\ j \neq i}}^N \left[-(1 - \delta) \frac{i}{3} \left(\frac{\epsilon - 1}{\epsilon + 2}\right) dx_j^3 \right] E_{y_j} \\ + \sum_{\substack{j=1 \\ j \neq i}}^N \left[(1 - s_i)\delta - (1 - \delta) \frac{i}{3} \left(\frac{\epsilon - 1}{\epsilon + 2}\right) ex_j^3 \right] E_{z_j} \\ = \frac{3}{\epsilon + 2} E_{z_{\text{inc},i}} \quad i = 1, 2, 3, \dots, N,\end{aligned}\quad (13)$$

where

$$\delta = \begin{cases} 0 & \text{if } i \neq j. \\ 1 & \text{if } i = j. \end{cases}$$

Equations (11)–(13) form a $3N \times 3N$ set of complex linear equations that we solved using LINPACK subroutines CGECO and CGESL, after which the scattered electric-field distribution at a far-field region was obtained by adding the contributions from N control volumes (primary spheres). This is expressed as:¹⁹

$$\mathbf{E}^d = \frac{k^2 \exp(ikr^d)}{\mathbf{r}^d} (1 - \mathbf{n}^d \mathbf{n}^d) \sum_j^N \exp(-ik\mathbf{n}^d \cdot \mathbf{r}^j) \alpha^j \mathbf{E}^j, \quad (14)$$

where \mathbf{r}^d is the distance and \mathbf{n}^d is the unit direction of the detector from the origin. After the total-scattered intensity is determined, intensities for left and right circularly polarized incident light are calculated. This is necessary to determine the scattering-matrix elements. To account for the presence of several particles with different orientations, an averaging procedure is followed with the methodology suggested by Singham *et al.*¹⁹ In this procedure, Euler angles are used to locate the positions of primary spheres at different orientations. By using the properties of the Euler transformation matrix, the equations are recast such that the inverse of the interaction matrix is found only once. The inverted matrix is then used to obtain scattering-matrix elements for different orientations of the soot agglomerate.

B. Components of the Mueller (Scattering) Matrix

The incident and scattered electric fields are related by¹⁰:

$$\begin{pmatrix} E_{\parallel s} \\ E_{\perp s} \end{pmatrix} = \frac{\exp[ik(r-z)]}{-ikr} \begin{pmatrix} S_2 & S_3 \\ S_4 & S_1 \end{pmatrix} \begin{pmatrix} E_{\parallel i} \\ E_{\perp i} \end{pmatrix}, \quad (15)$$

where S_1 , S_2 , S_3 , and S_4 form the amplitude-scattering matrix that depends on the scattering angle and the orientation of the particle with respect to the incident field vector. E_{\parallel} and E_{\perp} represent the parallel and perpendicular components of the electric field with respect to the plane of scattering, $k = 2\pi/\lambda$ is the wave number, and r is the distance from the center of the flame to the detector. Expressions that relate amplitude-scattering matrix elements to scattered field owing to left and right circularly polarized incident light are given by Singham *et al.*¹⁹

In experiments, the incident and scattered electric fields are not measured. Instead, it is preferable to relate these quantities to measurables such as irradiances:

$$\begin{pmatrix} I_s \\ Q_s \\ U_s \\ V_s \end{pmatrix} = \frac{1}{k^2 r^2} \begin{pmatrix} S_{11} & S_{12} & S_{13} & S_{14} \\ S_{21} & S_{22} & S_{23} & S_{24} \\ S_{31} & S_{32} & S_{33} & S_{34} \\ S_{41} & S_{42} & S_{43} & S_{44} \end{pmatrix} \begin{pmatrix} I_i \\ Q_i \\ U_i \\ V_i \end{pmatrix}, \quad (16)$$

or

$$[\mathbf{K}_s] = \frac{1}{k^2 r^2} [S][\mathbf{K}_i]. \quad (17)$$

Here, $[\mathbf{K}_i]$ and $[\mathbf{K}_s]$ are the incident and scattered intensity vectors, respectively. Their components, I , Q , U , and V , correspond to four measurable quantities: total intensity, linear horizontal or vertical polarized, linear $+45^\circ$ or -45° polarized, and right or left circularly polarized light intensity, respectively. The $[S]$ matrix is nothing more than the scattering (Mueller) matrix, and its components are related to the elements of the amplitude-scattering matrix in Eq. (15).¹⁰ Each matrix element is a function of scattering angle θ . The Mueller matrix for a cloud of particles is the sum of individual Mueller matrices for each particle.

Although there are 16 S_{ij} elements, only seven are independent. Depending on the symmetry of the scatterer, this matrix can be simplified even further. For a cloud of particles that has a plane of symmetry in which the particles are randomly oriented, the matrix reduces to⁴⁷

$$[S(\theta)] = \frac{1}{k^2 r^2} \begin{pmatrix} S_{11} & S_{12} & 0 & 0 \\ S_{12} & S_{22} & 0 & 0 \\ 0 & 0 & S_{33} & S_{34} \\ 0 & 0 & -S_{34} & S_{44} \end{pmatrix}. \quad (18)$$

Because soot particles and soot agglomerates in flames are randomly oriented, they can have a plane of symmetry. Hence the Mueller matrix for particles in flames consists of six independent parameters,

as given in Eq. (18). S_{11} is the differential-scattering cross section of the scatterer. If normalized by the area under the $S_{11} - \theta$ curve, S_{11} becomes the phase function of the scatterers (which is essential in estimating the distribution of radiation intensity in a medium containing scatterers). S_{12} is the measure of linearly polarized scattered light for an incident unpolarized light. In general, the angular pattern of S_{12} shows how much the agglomerate deviates from the Rayleigh scattering regime. S_{34} indicates how much of an obliquely polarized light (45°) is transformed to circularly polarized light because of the scatterer. S_{44} has an angular pattern similar to S_{33} .

4. Results and Discussions

We now present the scattering-matrix elements obtained for different soot agglomerates. A series of results is presented to help decide which matrix elements are to be measured and how sensitive the matrix elements are to the nature of a given agglomerate shape and structure. The section is divided into different subsections to highlight how the scattering matrix elements may change owing to variations in the morphology and the refractive index of soot agglomerates. The effect of wavelength of incident radiation on soot-agglomerate scattering characteristics is also investigated. Note that the change in wavelength affects the size parameter as well as the complex index of refraction of the soot particles. In all the figures presented, N is the total number of primary spheres in an agglomerate, d_p is the diameter of the primary sphere, λ is the wavelength of incident radiation, and m is the complex index of refraction of the agglomerate.

A. Validation of the Code

To validate the computer program AGGLOME, we first performed a series of calculations for spherical particles and compared the results to the corresponding Lorenz-Mie predictions. We constructed spherical particle using cubical control volumes. The edge of each cubical element of the cube is given a value of 0.75 units, and the radius of the sphere thus constructed is 3.0 units. This yields the radius of an equivalent sphere (based on volume) to be 2.95 units for the number of cubical volumes of $N = 257$. The size parameters considered are $x = 0.5$, 1.0, and 1.5. We obtained different size parameters by changing the wavelength of incident radiation. The refractive index for the sphere is assumed to be $1.33 - 0.0i$ at all the wavelengths considered.

The angular variations of S_{11} ($= S_{22}$), S_{12} ($= S_{21}$), S_{33} ($= S_{44}$), and S_{34} ($= S_{43}$) as predicted by the AGGLOME algorithm and Lorenz-Mie theory are depicted in Fig. 2. The trends and magnitudes of S_{11} , S_{12} , and S_{33} that we obtained using the AGGLOME agree well with the Mie sphere results for all the size parameters considered. On the other hand, for $x = 1.5$, the magnitude of S_{34} differs from that of the Mie sphere, even though the qualitative nature of the angular variation is preserved. The lack of good agreement in this case is due to the fact that S_{34} is

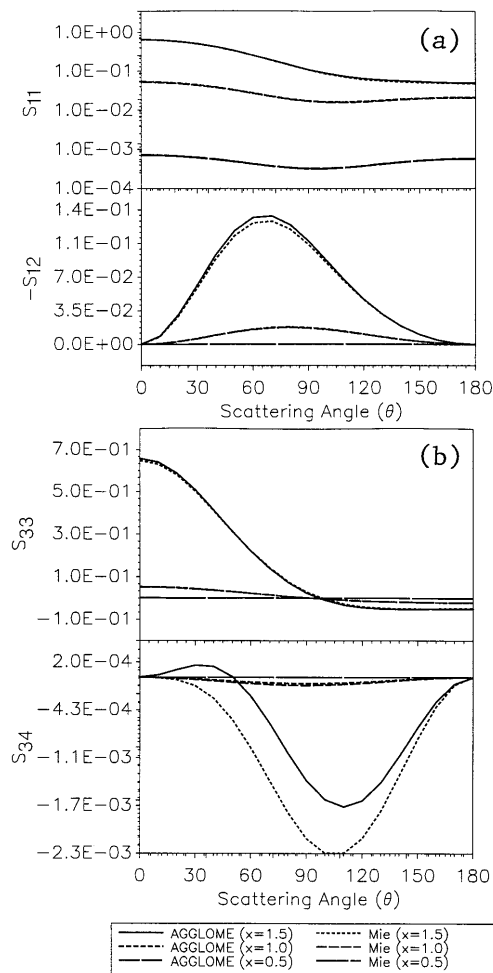


Fig. 2. Comparisons of the agglomerate results against the Lorenz-Mie calculations for spheres: (a) angular variations of S_{11} and S_{12} , (b) angular variations of S_{33} and S_{34} .

sensitive to the shape and to both the compactness and the granularity of the object. In our case, for $N = 257$, the constructed sphere does not represent the smooth Mie sphere quite accurately and hence the disagreement.

B. Generation of Agglomerates

To determine the scattering-matrix elements of soot agglomerates, it is essential that the agglomerates generated possess the structural properties of real soot in combustion systems. A detailed analysis of soot structure is presented by Samson *et al.*⁴⁸ in which experimental results on soot structure are compared with those obtained by the numerical simulations based on the diffusion-limited aggregation (DLA) and cluster-cluster aggregation (CCA) processes.

In this study we generated the agglomerates by a random process. The soot agglomerate is assumed to have a fractal dimension of 1.7 and a prefactor of 5.8. The process involved adding a single sphere at a time to a stationary sphere or cluster, with a restriction that the fractal dimension should remain

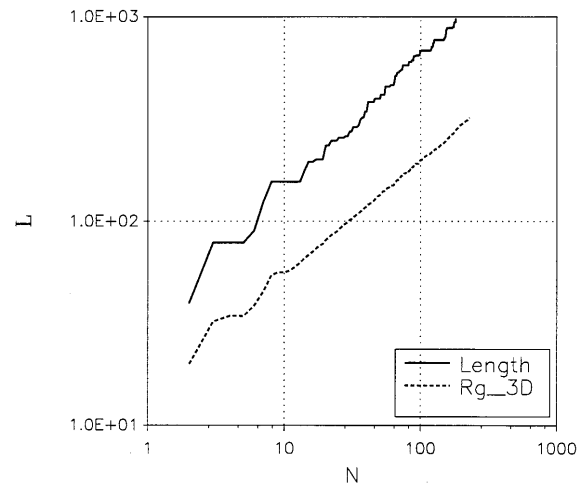


Fig. 3. Projected length and radius of gyration (three dimensional) as a function of N .

constant at 1.7. The position at which the sphere is attached during the simulation depended on this constraint. A similar approach was followed by Köylü *et al.*⁴⁹ in their study to determine the relation between the three-dimensional and projected images of soot agglomerates. Farias *et al.*⁵⁰ followed a similar simulation process while investigating the effect of polydispersity of aggregates on radiative properties of soot.

Various agglomerates with differing N (number of primary spheres) and d_p (diameter of primary spheres) generated for this study are shown in Fig. 1. Typical values of N used were 25, 50, 75, 100, 125, and 150, and values of d_p were 20, 40, and 60 nm. The wavelengths of the incident radiation were 266, 532, or 1000 nm (roughly corresponding to those of a Nd:YAG laser). The indices of refraction at these wavelengths are $1.076-0.688i$, $1.85-0.5i$, and $1.80-0.5i$, respectively.

Although the fractal dimension and the prefactor represent the soot-agglomerate structure, there is a possibility that the shape of the agglomerate generated will be different from that of real soot (which can be considered as a diffusion-limited cluster aggregate). If this is true, the results presented for the polarized light may not correspond to those to be measured in the experiments. Because of this it is desirable to investigate the soot structure and determine whether the basic characteristics of fractal representation change as a function of the observation plane.

To investigate if the simulated soot agglomerates have the open structure of the real soot, we estimated the projected properties as a function of N . Figure 3 shows the variation of maximum projected length L and the three-dimensional radius of gyration $R_{g,3d}$ as a function of N . Approximately 490 different orientations of the agglomerate are considered to determine the maximum projected length. Figure 3 indicates that the fractal dimension of the projected agglomerate is closer to that of the three-dimensional

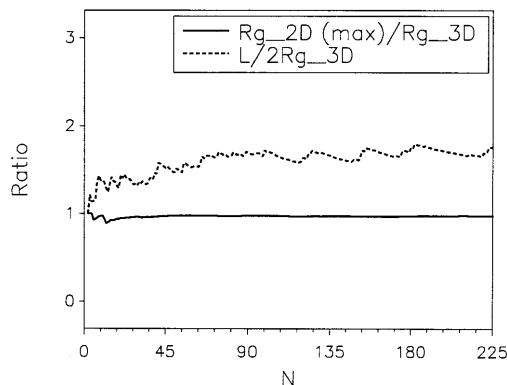


Fig. 4. Projected length and maximum radius of gyration (two dimensional) normalized with respect to radius of gyration (three dimensional) as a function of N .

case. Figure 4 depicts the variation of $R_{g,2d}(\max)/R_{g,3d}$ and $L/2R_{g,3d}$ ratios as a function of N . Although the ratios of radii of gyration remain more or less constant at ~ 0.99 , $L/2R_{g,3d}$ increases with N and then asymptotically approaches a constant value. Note that one can evaluate $R_{g,2d}(\max)$ by considering several different orientations of the agglomerate and the corresponding projections.

Figure 5 shows the radius of gyration for 25 different random projections of the agglomerate ($R_{g,2d}$) as a function of N . It is clear that the projected images of the agglomerates have practically the same fractal dimensions at different planes of projections. This is

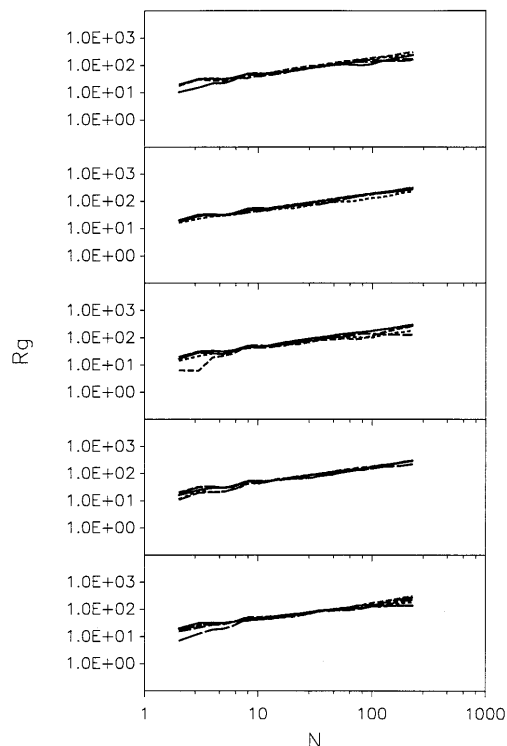


Fig. 5. Radius of gyration (two dimensional) for 25 different orientations as a function of N (plotted in five separate frames for clarity).

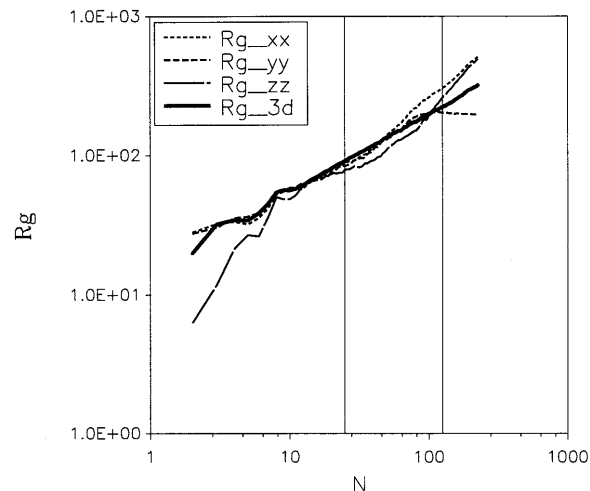


Fig. 6. Principal radii of gyration (three dimensional) as a function of N . Vertical lines show the range of N values considered.

possible only if the soot agglomerate generated has an open structure in all directions. Figure 6 depicts the variation of principal radii of gyration and $R_{g,3d}$ as a function of N . Note that in the range considered here, the variation is linear (in log scale) and the lines fall on top of each other. This indicates that, even though the agglomerates are generated based on a random process, they look similar as viewed from different axes. Thus with the fractal dimension fixed the restricted growth of the agglomerate by the random process has not resulted in an agglomerate that is different from real soot.

In this study, the scattering-matrix elements are obtained after several different orientations are averaged and, consequently, structure effects on the results are minimized. In addition, when there is a size distribution of agglomerates, shape effects are further reduced. This does not imply that soot agglomerates can be modeled as, for example, equivalent solid spheres. Our objective here is not to investigate the structure of soot but rather to employ simplified means to simulate the soot agglomerate and study its scattering characteristics. Therefore the approach followed here in generating the soot-agglomerate structures is acceptable; additional studies with regard to CCA or DLA approaches should be performed, however.

C. Effect of Orientational Averaging

One can perform orientational averaging by rotating the incident field vector with respect to the particle. This method eliminates the need to find the inverse of the interaction matrix for each orientation (Singham *et al.*¹⁹). The system of equations [Eqs. (11)–(13)] derived earlier in this study can be represented in matrix form as

$$[A][E_s] = [E_i], \quad (19)$$

which can be rewritten as

$$[E_s] = [A^{-1}][E_i]. \quad (20)$$

The effect of rotating the particle can be expressed using the Euler transformation matrix for rotation.⁵¹ If O denotes the Euler matrix, the following transformations are observed when the particle is rotated¹⁹:

$$\mathbf{r}'^i = O^T \mathbf{r}^i, \quad (21)$$

$$\hat{n}'^j = O^T \hat{n}^j, \quad (22)$$

$$\alpha'^j = O^T \alpha^j O. \quad (23)$$

Here α is the polarization tensor, \mathbf{r} is the position vector, and \hat{n}^j is the unit vector in the direction from j to i , where j and i indicate two different control volumes. These relations are substituted in the governing equation (in matrix form) and rearranged. It is found that A^{-1} , which appears in Eq. (20), is independent of rotation angles whereas the matrices that correspond to the incident field vector are changed.

As the agglomerate is rotated, the coordinates of the centers of the control volumes are changed. This results in a change in position vectors of different control volumes. The position vectors determine how much each control volume contributes to the total scattered field. However, with the properties of the transformation matrix (O) the changes are accommodated by rotating the incident-field vector. This means that the inverse of the interaction matrix A is found only once and is used to determine the scattered electric-field vector for all orientations of the incident field. Then, the Euler transformation of the solution and the numerical averaging over the solid angles yield a resultant electric field at various locations inside the agglomerate.

The number of orientations required to obtain accurate results depends on the size of the particle compared with the wavelength of the incident radiation. In this study, the most sensitive case ($\lambda = 266$ nm and $N = 150$) determines the number of orientations for all other cases studied. It is also found that S_{12} and S_{34} are the elements most sensitive to the number of orientations. Hence convergence of these two matrix elements within reasonable accuracy is given importance in the determination of the minimum number of orientations required in the calculations.

Figure 7 shows the effect of the number of orientations considered on the magnitude of S_{12} and S_{34} . M corresponds to the number of orientations in each of the Euler angle directions. For example, $M = M_\phi \times M_\theta \times M_\psi$ indicates the number of orientations in the ϕ , θ , and ψ directions. From the figure we conclude that the results for the number of orientations of $10 \times 6 \times 6$ and of $10 \times 7 \times 7$ are similar. Based on this, we inferred that the convergence is achieved for $M = 10 \times 7 \times 7$, and we used it for the rest of the calculations. Hence 490 orientations are considered in the determination of the orientationally averaged values of all scattering-matrix elements (S_{11} converged much faster than other elements in all cases).

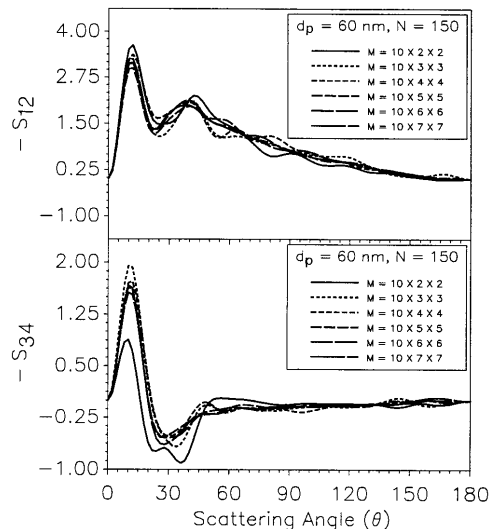


Fig. 7. Angular variation of S_{12} and S_{34} for various orientations of the agglomerate.

D. Effects of N and d_p

1. S_{11}

Figures 8, 9, and 10 depict the angular variation of S_{11} as a function of N and d_p at wavelengths of 266, 532, and 1000 nm, respectively. For each wavelength the value of S_{11} near the forward directions increases 1 order of magnitude as d_p varies from 20 to 40 nm and then to 60 nm. This sensitivity suggests that an experimental technique can be developed to obtain the values of N and d_p . It is also possible for one to determine the fractal dimension of soot agglomerates by measuring the angular variation of

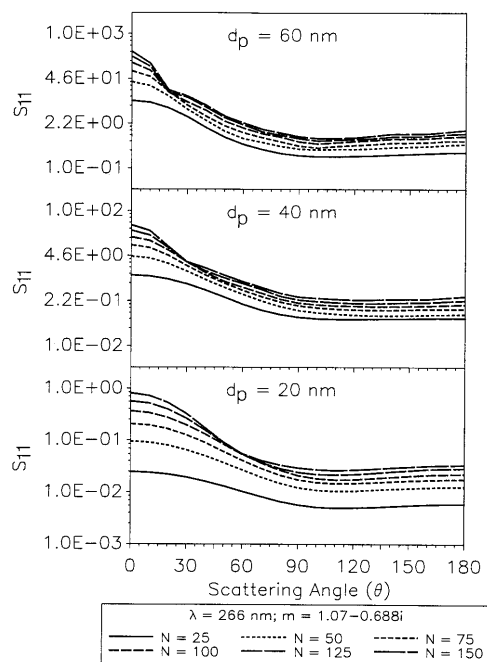


Fig. 8. Effect of N and d_p on the angular profile of S_{11} elements: $\lambda = 266$ nm, $m = 1.07-0.688i$.

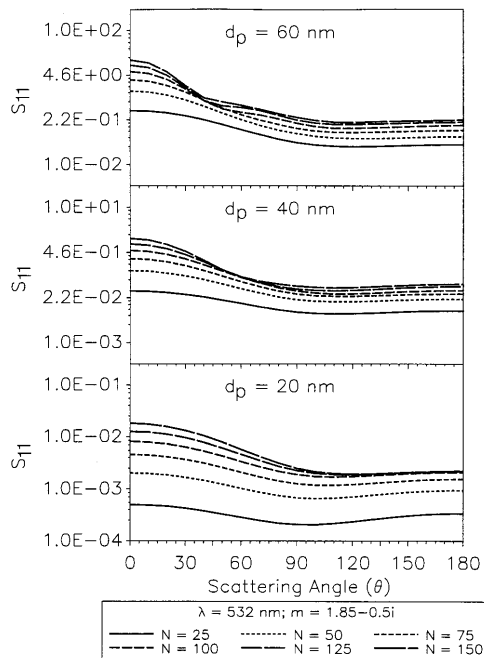


Fig. 9. Effect of N and d_p on the angular profile of S_{11} elements: $\lambda = 532$ nm, $m = 1.85-0.50i$.

S_{11} . However, a close examination of these figures shows some possible pitfalls. One pitfall is the possible nonuniqueness in the predictions. For example, in Fig. 8 the angular variations of S_{11} at $\lambda = 266$ nm and for $N = 75$ or 100 ($d_p = 40$ nm) are almost the same as the angular pattern for $N = 25$ ($d_p = 60$ nm), which means that a soot agglomerate of a diameter of 60 nm composed of 25 primary spheres will scatter

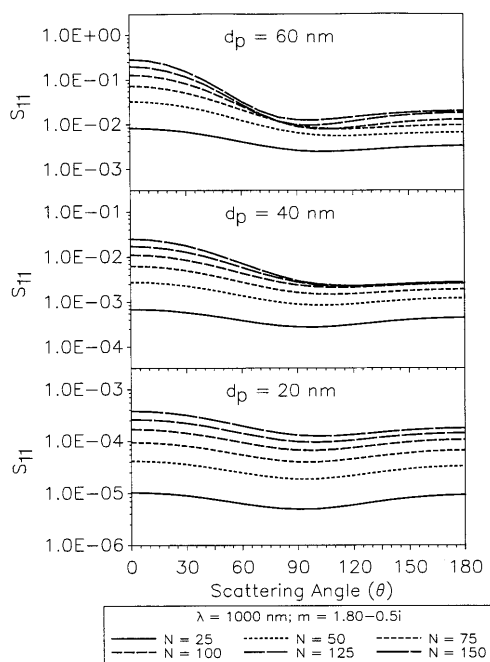


Fig. 10. Effect of N and d_p on the angular profile of S_{11} elements: $\lambda = 1000$ nm, $m = 1.80-0.50i$.

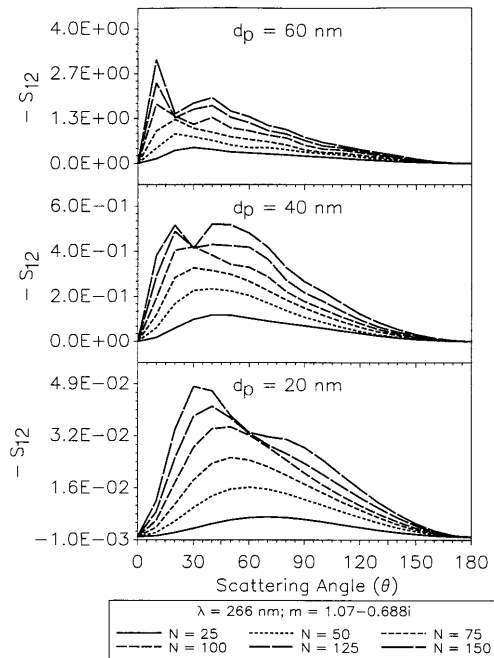


Fig. 11. Effect of N and d_p on the angular profile of S_{12} elements: $\lambda = 266$ nm, $m = 1.07-0.688i$.

incident radiation similar to a 75- or 100-sphere agglomerate with $d_p = 40$ nm. Even if we compare the total scattered energy for these agglomerates (area under S_{11}), which will be their scattering coefficients, the difference will not be large enough to determine either N or d_p accurately.

2. S_{12}

The angular variation of S_{12} for various N , d_p , and λ values is shown in Figs. 11–13. The maxima of S_{12} gradually shifts from near 60° to forward angles as N increases. The same behavior is observed for an increase in d_p (at a fixed wavelength). For example, in Fig. 11 the maxima occurs near 45° for $N = 75$ for $d_p = 20$ nm. As d_p changes to 40 nm (for $N = 75$), the maxima shifts to angles slightly smaller than 30° . This suggests a possible diagnosis of N if we know the primary sphere diameter (d_p) *a priori*. If measurements are made at 1000 nm, it is possible to estimate the primary sphere diameter. It can be observed from Fig. 13 that, at the wavelength of 1000 nm, the S_{12} profile becomes asymmetric around 90° as d_p increases, whereas for $d_p = 20$ nm there is almost perfect symmetry around 90° . A diagnostic technique based on multiwavelength scattering measurements may yield both N and d_p .

3. S_{33}

Figures 14–16 depict the angular behavior of S_{33} (or S_{44}) at various wavelengths as a function of N and d_p . As N increases, the S_{33} peaks toward the forward angles. In other words, if we take the area under a typical S_{33} curve, the ratio of area in the forward direction to area in the backward angles (greater than 90°) becomes a strong function of d_p and N ,

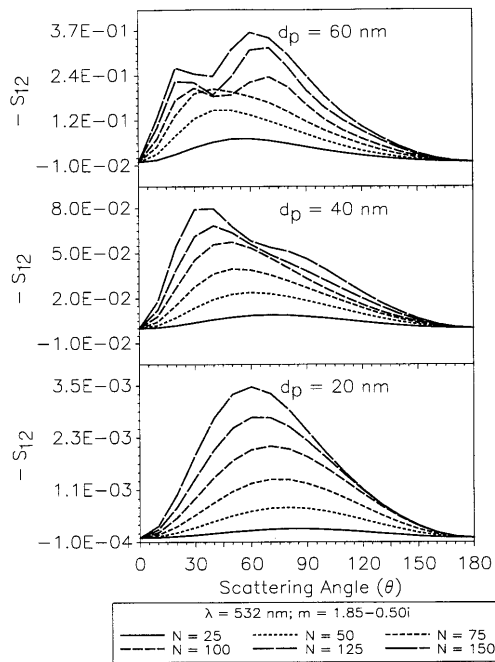


Fig. 12. Effect of N and d_p on the angular profile of S_{12} elements: $\lambda = 532$ nm, $m = 1.85-0.50i$.

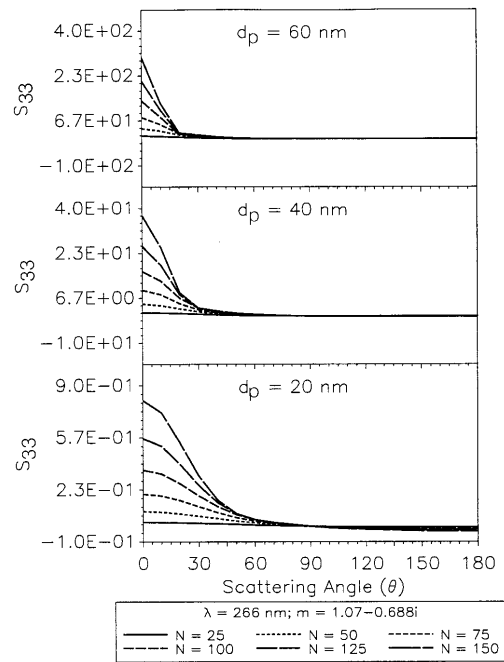


Fig. 14. Effect of N and d_p on the angular profile of S_{33} elements: $\lambda = 266$ nm, $m = 1.07-0.688i$.

particularly at short wavelengths (such as 266 nm). At the wavelength of 1000 nm, where the angular pattern of S_{33} loses its symmetry as d_p increases, it is possible to identify the primary-sphere diameter with reasonable accuracy.

Figure 17 shows the asymmetry ratio for S_{33} at wavelengths of 532 and 1000 nm. The asymmetry ratio is calculated as the ratio of total forward-

scattered light to that of backscattered light (greater than 90°). This ratio increases as d_p and N increase at both wavelengths. Note that there is a non-unique combination of N and d_p that yields the same value of the asymmetry ratio if these wavelengths are considered. However, if we take into account the spectral variation of the asymmetry ratio, then it provides a unique combination of N and d_p .

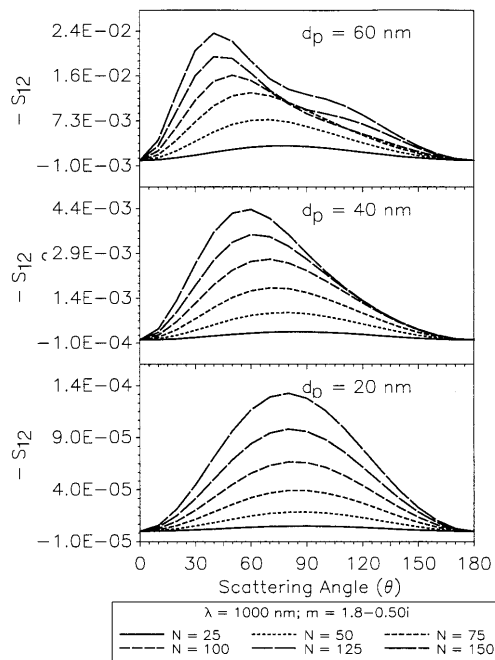


Fig. 13. Effect of N and d_p on the angular profile of S_{12} elements: $\lambda = 1000$ nm, $m = 1.8-0.50i$.

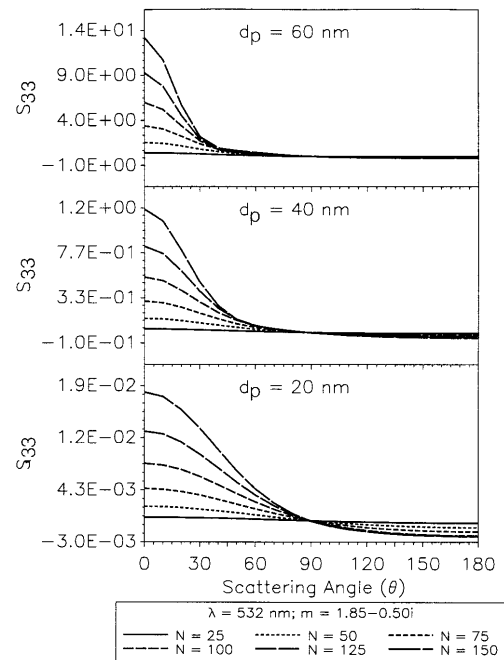


Fig. 15. Effect of N and d_p on the angular profile of S_{33} elements: $\lambda = 532$ nm, $m = 1.85-0.50i$.

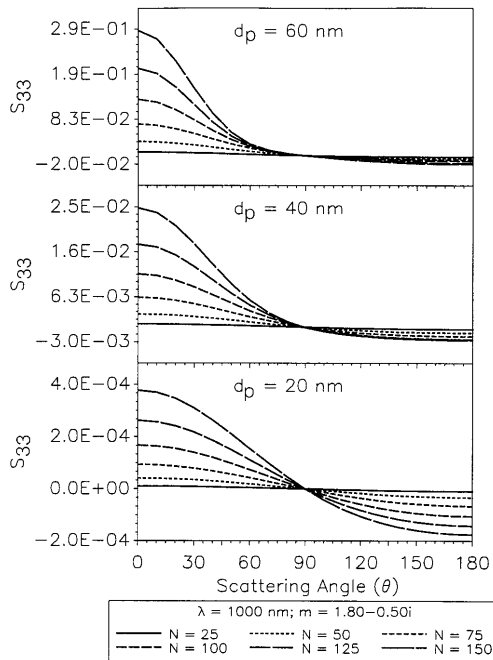


Fig. 16. Effect of N and d_p on the angular profile of S_{33} elements: $\lambda = 1000$ nm, $m = 1.80-0.50i$.

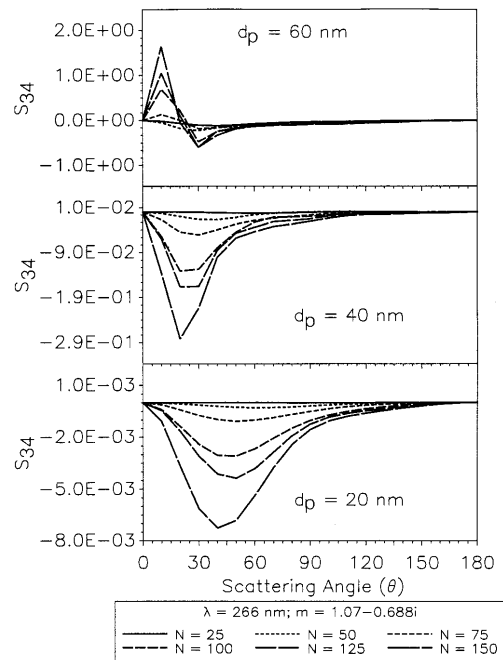


Fig. 18. Effect of N and d_p on the angular profile of S_{34} elements: $\lambda = 266$ nm, $m = 1.07-0.688i$.

4. S_{34}

The angular pattern of S_{34} as a function of wavelength and N are displayed in Figs. 18–20. S_{34} has some unique features that were not observed for other elements. For a given wavelength and a primary-sphere diameter a minimum can be noted for various N at about the same scattering angle. In other words the angle at which this minimum occurs is

a strong function of d_p but not of N . For example, in Fig. 18 ($\lambda = 266$ nm, $d_p = 20$ nm) the minima occurs at angles close to 45° , whereas for $\lambda = 266$ nm and $d_p = 40$ nm the minima occurs near 20° . In the case of $d_p = 60$ nm a bimodal profile is observed; the maxima occurs near 15° and the minima at around 30° . A similar trend can be noted at the wavelength of 532 nm (Figs. 19 and 20). Thus the nonuniqueness that

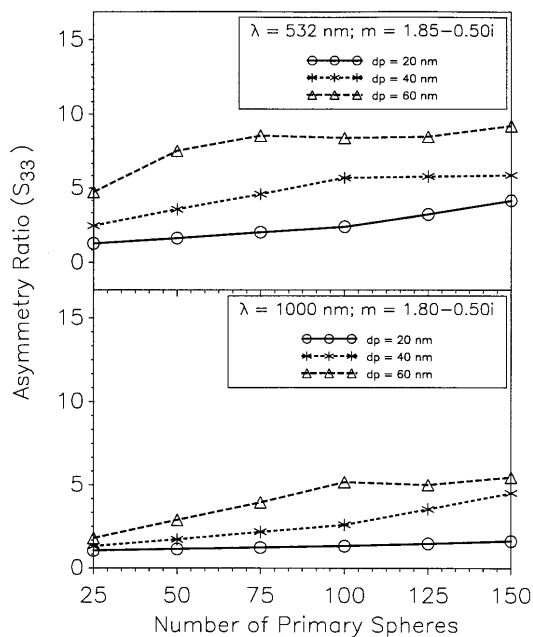


Fig. 17. Ratio of total forward-scattered light to backward-scattered light (asymmetry ratio) based on S_{33} at $\lambda = 532$ and 1000 nm.

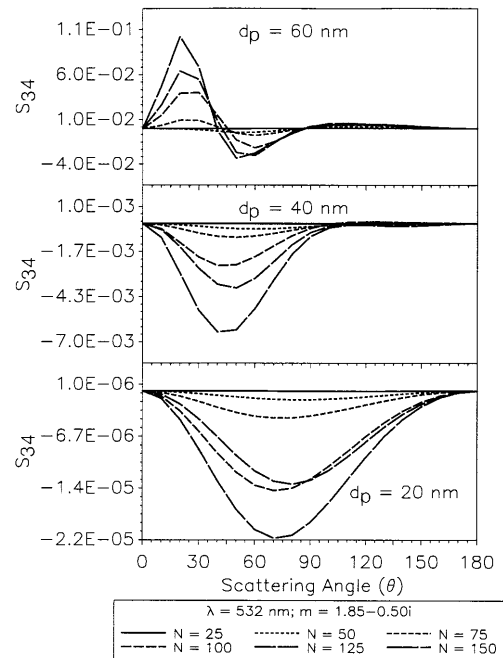


Fig. 19. Effect of N and d_p on the angular profile of S_{34} elements: $\lambda = 532$ nm, $m = 1.85-0.50i$.

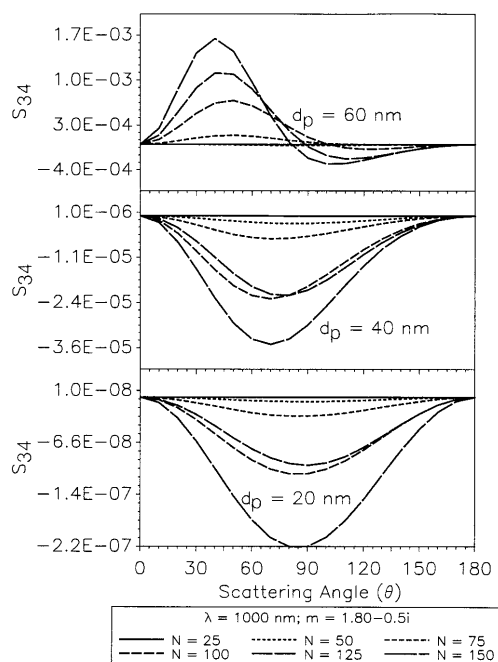


Fig. 20. Effect of N and d_p on the angular profile of S_{34} elements: $\lambda = 1000$ nm, $m = 1.80 - 0.50i$.

we discussed in the earlier section can be removed if we can measure angular variation of S_{34} accurately (which is unfortunately not easy).

5. Other S_{ij} Elements

We have not discussed the behavior of other elements of the Mueller matrix (S_{22} and S_{44}) because their behaviors are comparable with those of S_{11} and S_{33} , respectively. In the calculations the ratio of S_{22} to S_{11} varied between 1 and 0.97, which indicates nonspherical behavior. Because our objective is not just to present the scattering matrix elements but to investigate their trends and their possible use for determining the physical nature of the agglomerates, discussions on these elements are excluded here.

5. Conclusions

On the basis of the results we presented, we can suggest a measurement strategy to obtain the morphological characteristics of soot agglomerates.

- The measurement of S_{11} (or the phase function) alone cannot be used to identify soot-agglomerate characteristics uniquely.

- It is possible for one to determine the individual sphere diameter d_p by making spectral and angular measurements of S_{12} . This information combined with measurements performed for angular variations of S_{11} can be used to determine the number of spheres N . On the other hand, if d_p is determined from electron-microscope images, it is possible with a detailed inverse technique to determine the polydispersity of agglomerates from measurements made on S_{11} and S_{12} .

- We have pointed out that S_{34} has some unique features that other matrix elements do not possess. The location of extrema in the angular variation of S_{34} at a given wavelength is a strong function of d_p and not of N , even for a polydispersed system of agglomerates. Hence this behavior can be used to determine uniquely the primary-sphere diameter of soot agglomerates. Yet S_{34} is sensitive to many physical variations, and its magnitude is usually small. Therefore it is not easy to develop a diagnostic technique based on S_{34} .

- Matrix elements such as S_{11} , S_{12} , and S_{33} can be measured to obtain the value of N after d_p is determined. In the case of a polydispersed system more parameters are to be recovered from experimental data; therefore more accurate angular and spectral measurements must be made. By measuring both S_{11} and S_{12} , one can compare the results obtained from inverse analyses on both set of measurements. This would serve as an additional validation for the experimental system and the inversion procedure.

The focus here has been on monodispersed agglomerates. Polydispersed systems are to be considered in a later study. In a parallel study,⁵² we have demonstrated the feasibility of measuring the absolute quantities of scattering-matrix elements.

This research has been partially supported by the Department of Energy, Pittsburgh Energy Technology Center, Advanced University Coal Research Program grants DE-FG22-PC92533 and DE-FG22-PC93210. The authors acknowledge the help of Stig Rene Alstedt, who simulated agglomerate structures used in the analysis. The constructive criticism of anonymous reviewers improved the paper significantly; their time and effort are appreciated.

References

1. A. D'Alessio, "Laser light scattering and fluorescence diagnostics of rich flames produced by gaseous and liquid fuel," in *Particulate Carbon: Formation during Combustion*, D. C. Siegl and G. W. Smith, eds. (Plenum, New York, 1981), p. 207.
2. B. S. Haynes and H. G. Wagner, "Soot formation," *Prog. Energy Combust. Sci.* **7**, 229–273 (1981).
3. P. Menna and A. D'Alessio, "Light scattering and extinction coefficient for soot forming flames in the wavelength range from 200 nm to 600 nm," in *Nineteenth Symposium (International) on Combustion* (The Combustion Institute, Pittsburgh, Pa., 1982), p. 1482.
4. T. T. Charalampopoulos, "Morphology and dynamics of agglomerated particulates in combustion systems using light scattering techniques," *Prog. Energy Combust. Sci.* **18**, 13–45 (1992).
5. R. A. Dobbins and C. M. Megaridis, "Morphology of flame generated soot as determined by thermophoretic sampling," *Langmuir* **3**, 254 (1987).
6. K. Saito, A. S. Gordon, F. A. Williams, and W. F. Stickley, "A study of the early history of soot formation in various hydrocarbon diffusion flames," *Combust. Sci. Technol.* **80**, 103–119 (1991).
7. S. Venkatesh, "Effect of chlorine on soot formation in laminar hydrocarbon diffusion flames," Ph.D. dissertation (Department

- of Mechanical Engineering, University of Kentucky, Lexington, Ky 1992).
8. C. M. Sorensen, J. Cai, and N. Lu, "Light-scattering measurements of monomer size, monomers per aggregate, and fractal dimension for soot aggregates in flames," *Appl. Opt.* **31**, 6547–6557 (1992).
 9. Ü. O. Köylü and G. M. Faeth, "Optical properties of soot in buoyant laminar diffusion flames," *J. Heat Transfer* **116**, 971–979 (1994).
 10. C. F. Bohren and E. R. Huffman, *Absorption and Scattering of Light by Small Particles*, (Wiley, New York, 1983).
 11. M. F. Iskander, H. Y. Chen, and J. E. Penner, "Optical scattering and absorption by branched-chains of aerosols," *Appl. Opt.* **28**, 3083–3091 (1989).
 12. S. B. Singham and G. C. Salzman, "Evaluation of the scattering matrix of an arbitrary particle using the coupled dipole approximation," *J. Chem. Phys.* **84**, 2658–2667 (1986).
 13. E. M. Purcell and C. R. Pennypacker, "Scattering and absorption by non-spherical dielectric grains," *Astrophys. J.* **186**, 705–714 (1973).
 14. P. R. Shapiro, "Interstellar polarization: magnetite dust," *Astrophys. J.* **201**, 151–164 (1975).
 15. S. D. Druger, M. Kerker, D. S. Wang, and D. D. Cooke, "Light scattering by inhomogeneous particles," *Appl. Opt.* **18**, 3888–3889 (1979).
 16. G. W. Kattawar and T. J. Humphreys, "Electromagnetic scattering from two identical pseudospheres," in *Light Scattering by Irregularly Shaped Particles*, D. W. Schuerman, ed. (Plenum, New York, 1980), pp. 177–190.
 17. Y. L. Yung, "Variational principles for scattering of light by dielectric particles," *Appl. Opt.* **17**, 3707–3709 (1978).
 18. S. B. Singham, "Intrinsic optical activity in light scattering from an arbitrary particle," *Chem. Phys. Lett.* **130**, 139–144 (1986).
 19. M. K. Singham, S. B. Singham, and G. C. Salzman, "The scattering matrix for randomly oriented particles," *J. Chem. Phys.* **85**, 3807–3815 (1986).
 20. S. B. Singham, C. W. Patterson, and G. C. Salzman, "Polarizabilities for light scattering from chiral particles," *J. Chem. Phys.* **85**, 763–770 (1986).
 21. V. V. Varadan, A. Lakhtakia, and V. K. Varadan, "Scattering by three-dimensional anisotropic scatterers," *IEEE Trans. Antennas Propag.* **37**, 800–811 (1989).
 22. A. Lakhtakia, R. Messier, V. V. Varadan, and V. K. Varadan, "Fractal dimension from the back-scattering cross section," *J. Phys. A: Math. Nucl. Gen.* **20**, 1615–1619 (1987).
 23. S. B. Singham and C. F. Bohren, "Light scattering by an arbitrary particle: the scattering order formulation of the coupled-dipole method," *J. Opt. Soc. Am. A* **5**, 1867–1872 (1988).
 24. C. E. Dungey and C. F. Bohren, "Light scattering by non-spherical particles: a refinement to the coupled-dipole method," *J. Opt. Soc. Am. A* **8**, 81–87 (1991).
 25. B. T. Draine, "The discrete-dipole approximation and its application to interstellar graphite grains," *Astrophys. J.* **333**, 848–872 (1988).
 26. A. Lakhtakia, "Macroscopic theory of the coupled dipole approximation method," *Opt. Commun.* **79**, 1–5 (1990).
 27. J. I. Hage and J. M. Greenberg, "Optics of fluffy particles," in *Proceedings of the Second International Congress on Optical Particle Sizing*, E. D. Hirtleman, ed. (Arizona State University, Tempe, Ariz., 1990), pp. 80–89.
 28. P. J. Flatau, G. L. Stephens, and B. T. Draine, "Light scattering by rectangular solids in the discrete-dipole approximation: a new algorithm exploiting the Block-Toeplitz structure," *J. Opt. Soc. Am. A* **7**, 593–600 (1990).
 29. M. P. Mengüç, A. Mahadeviah, K. Saito, and S. Manickavasagam, "Application of the discrete dipole approximation to determine the radiative properties of soot agglomerates," in *Heat Transfer in Fire and Combustion Systems*, A. M. Kanury and M. Q. Brewster, eds., (American Society of Mechanical Engineers, New York, 1992), pp. 9–16.
 30. B. T. Draine and P. J. Flatau, "The discrete-dipole approximation for scattering calculations," *J. Opt. Soc. Am. A* **11**, 1491–1499 (1994).
 31. D. W. Mackowski, "Calculation of total cross sections of multiple-sphere clusters," *J. Opt. Soc. Am. A* **11**, 2851–2861 (1994).
 32. K. A. Fuller, "Scattering and absorption cross sections of compounded spheres. I. Theory for external aggregation," *J. Opt. Soc. Am. A* **11**, 3251–3260 (1994).
 33. A. R. Jones, "Electromagnetic wave scattering by assemblies of particles in the Rayleigh approximation," *Proc. R. Soc. London Ser. A* **366**, 111–127 (1979); corrections in **375**, 453–454 (1979).
 34. A. R. Jones, "Scattering efficiency factors for agglomerates of small spheres," *J. Phys. D* **12**, 1661–1672 (1979).
 35. J. D. Felske, P. F. Hsu, and J. C. Ku, "The effect of soot particle optical inhomogeneity and agglomeration on the analysis of light scattering measurements in flames," *J. Quant. Spectrosc. Radiat. Transfer* **35**, 447 (1986).
 36. B. L. Drolen and C. L. Tien, "Absorption and scattering of agglomerated soot particulate," *J. Quant. Spectrosc. Radiat. Transfer* **37**, 433–448 (1987).
 37. S. Kumar and C. L. Tien, "Dependent scattering and absorption of radiation by small particles," in *Fundamentals and Applications of Radiation Heat Transfer*, A. M. Smith, ed. [American Society of Mechanical Engineers, New York, 1987], pp. 1–7.
 38. D. W. Mackowski, R. A. Altenkirch, M. P. Mengüç, and K. Saito, "Radiative properties of chain-agglomerated soot formed in hydrocarbon diffusion flames," in *Twenty-Second Symposium (International) on Combustion* (The Combustion Institute, Pittsburgh, Pa., 1988) p. 1263.
 39. J. C. Ku and K. H. Shim, "The effects of refractive indices, size distribution and agglomeration on the diagnostics and radiative properties of flame soot particles," in *Heat and Mass Transfer in Fires and Combustion Systems*, HTD Vol. 148, W. L. Grosshandler and H. G. Semerjian, eds., (American Society of Mechanical Engineers, New York, 1990), pp. 105–115.
 40. J. C. Ku and K. H. Shim, "A comparison of solutions for light scattering and absorption by agglomerated or arbitrarily-shaped particles," *J. Quant. Spectrosc. Radiat. Transfer* **47**, 201–220 (1992).
 41. T. T. Charalampopoulos and H. Chang, "Agglomerate parameters and fractal dimension of soot using light scattering: effects on surface growth," *Combust. Flame* **87**, 89–99 (1991).
 42. S. K. Forrest and T. A. Witten, Jr., "Long-range correlations in smoke-particle aggregates," *J. Phys. A: Math. Nucl. Gen.* **12**, 109–117 (1979).
 43. I. Colbeck, E. J. Hardman, and R. M. Harrison, "Optical and dynamical properties of fractal clusters of carbonaceous smoke," *J. Aerosol Sci.* **20**, 765–774 (1989).
 44. J. Nelson, "Test of a mean field theory for the optics of fractal clusters," *J. Mod. Opt.* **36**, 1031–1057 (1989).
 45. C. M. Megaridis and R. A. Dobbins, "Morphological description of flame-generated materials," *Combust. Sci. Technol.* **71**, 95–109 (1990).
 46. G. H. Goedecke and S. G. O'Brien, "Scattering by irregular inhomogeneous particles via the digitized Green's function algorithm," *Appl. Opt.* **27**, 2431–2438 (1988).

47. H. C. van de Hulst, *Light Scattering by Small Particles* (Dover, New York, 1981), pp. 46–50.
48. R. J. Samson, G. W. Mulholland, and J. W. Gentry, “Structural analysis of soot agglomerates,” *Langmuir* **3**, 272–281 (1987).
49. Ü. Ö. Köylü, G. M. Faeth, T. L. Farias, and M. G. Carvalho, “Fractal and projected structure properties of soot aggregates,” *Combust. Flame* **100**, 621–633 (1995).
50. T. L. Farias, Ü. Ö. Köylü, and M. G. Carvalho, “Effects of polydispersity of aggregates and primary particles on radiative properties of simulated soot,” *J. Quant. Spectrosc. Radiat. Transfer* **55**, 357–371 (1995).
51. H. Goldstein, *Classical Mechanics* (Addison-Wesley, Reading, Mass., 1980), pp. 143–148.
52. R. Govindan, S. Manickavasagam, and M. P. Mengüç, “Measuring the Mueller matrix elements of soot agglomerates,” in *Radiative Transfer I: Proceedings of International Symposium on Radiative Heat Transfer*, M. P. Mengüç, ed. (Begell House, New York, 1996), pp. 280–295.